PCCP

Accepted Manuscript

ROYAL SOCIETY OF CHEMISTRY

www.rsc.org/pccp

PCCP

Paper

Structure-Barrier Property Relationship of Biodegradable Poly(butylene succinate) and Poly[(butylene succinate)-co-(butylene adipate)] Nanocomposites : Influence of the Rigid Amorphous Fraction

Received 00th January 20xx,
Accepted 00th January 20xx

DOI: 10.1039/x0xx00000x

www.rsc.org/

S. Charlon[a,b,], S. Marais[*a,b,c], E. Dargent[a,d], J. Soulestin[e], M. Sclavons[f], N. Follain[a,b,c]

Composites composed of polyesters, Poly(Butylene Succinate) (PBS) or Poly[(Butylene Succinate)-co-(butytlene Adipate)] (PBSA), and 5 wt% of montmorillonite (CNa) or organo-modified montmorillonite (C30B) were melt-processed and transformed into films by either compression-molding or extrusion-calendering. XRD, rheological measurements and TEM images clearly indicated that films containing CNa are microcomposites, while nanocomposites were observed for those containing C30B. Using Flash DSC, it was possible, for the first time, not only to measure the heat capacity step at the glass transition of these two materials in their amorphous state, but also to investigate whether the preparation technique influenced the Rigid Amorphous Fraction (RAF) in our PBS- and PBSA-based nanocomposites. In this work, we have successfully shown the correlation between the microstructure of the films and their barrier properties, and especially the role played by the RAF. Indeed, the lowest permeabilities to gases and to water were determined in the films containing the highest RAF in both PBS- and PBSA-based materials.

Introduction

Emerging environmental concerns, have focused much research work on biodegradable polymers, with the aim of reducing plastic pollution. Indeed, due to their long lifetime, common polyolefins induce various forms of pollution, especially in the marine environment[1]. Eco-friendly materials such as biopolyesters seem to be of great interest [2,3] because they generally break down rapidly in water, carbon dioxide and humus under aerobic conditions, with the presence of microorganisms. Among these materials, Poly(Butylene Succinate) (PBS) and Poly[(Butylene Succinate)-co-(butytlene Adipate)] (PBSA) are especially promising. Indeed, their biodegradability[4], their good processability, similar to common thermoplastics[5] their chemical resistance, their mechanical properties, comparable to polypropylene[6] and their thermal properties[7] make them interesting alternatives to conventional plastics in industrial applications. However, as they are soft materials, with barrier properties that are not as efficient as those of polyethylene and polypropylene[8], for some applications, such as packaging, their use is limited.

Incorporating nanofillers into biopolyesters is one way to improve their physico-chemical properties, mainly their thermo-mechanical[9] and barrier properties[10]. It has already been reported that loading polymers with only a small amount of clay filler (3-5 wt%[4,11] significantly enhances their properties. The great benefit of the nanofiller montmorillonite is its high aspect ratio, greater than 100, which offers a large contact area with polymer chains. Moreover, clays are cheap, naturally abundant and environmentally-friendly.

To optimize the performances of nanocomposites, it is essential, in order to prevent filler aggregates forming, to increase as much as possible the levels of exfoliation and dispersion of nanoclays in polymer matrices. The control of these levels depends highly on the nanofiller chosen and the adequate preparation process. In the literature, the most frequently used nanoclay is montmorillonite (MMT)[12] and especially the organo-modified montmorillonite (OMMT)[13]. Due to its high polarity, the difficulty of dispersing and exfoliating MMT in organic matrices has often been reported[11,14]. Cations at the MMT surface are thus often substituted by surfactants which decrease the nanofiller polarity and increase the interfoliar space. The resulting OMMT is usually the best choice for the preparation of nanocomposites but unlike MMT, which is thermally stable, the onset degradation temperature of OMMT is often lower than 200 °C[15], depending on the chemical nature of the surfactant. OMMT can, moreover, promote random degradation of polymer chains, thus reducing the properties of a material[16]. An adequate preparation process could improve the dispersion and exfoliation levels of MMT, so that the organo-modification step would no longer be necessary. Composite films are usually made by

---

[a] *Normandie Univ. France*
[b] *Université de Rouen, PBS laboratory, F-76821 Mont-Saint-Aignan Cedex, France*
[c] *UMR 6270 CNRS & FR 3038 INC3M, F-76821 Mont-Saint-Aignan Cedex, France*
[d] *AMME-LECAP laboratory EA 4528, F-76800 Saint-Etienne du Rouvray, France*
[e] *Mines Douai, Department of Polymers and Composites Technology and Mechanical Engineering, F-59508 Douai, France*
[f] *Louvain la Neuve Catholic University, IMCN Institute, 1348 Louvain-La-Neuve, Belgium*

one of three methods: swelling in solvent, in-situ polymerization and melt-intercalation. Only the last method is considered environmentally-friendly, because it does not require the use of any solvent. However, this method can present some risks in preparing nanocomposite materials[17] as nanoparticles are harmful to human health. The inhalation of nanoclays for a long time can induce several pathologies such as cancer or pneumoconiosis[18]. Therefore, strong and specific protection equipments have to be used during the nanocomposite preparation. The melt intercalation is often applied with polymers having good processability properties, and the samples are generally formed using injection-molding[19,20] or compression-molding[21,22]. Extrusion-calendering is not often used for preparing composites, although it is a process that can orientate the nanofillers in the direction of the extrusion pathway.

In this work, composites composed of either a PBS or a PBSA polymer matrix and of native or organo-modified montmorillonite were prepared. Nanofillers were incorporated at the optimized 5 wt% content[23]. The composite films were made either by compression-molding or by extrusion-calendering. The efficiency of the process used was investigated by analyzing the transport properties of both types of composites.

The fundamental aim of this study was to investigate how the microstructures of our materials influenced their barrier properties. These microstructures from two semi-crystalline polymers (PBS and PBSA), differing in their degrees of crystallinity, were varied by incorporating 5 wt% of two different fillers (MMT and OMMT) by means of two different processes (thermo-molding and extrusion-calendering).

For a better insight into microstructure-transport property relationships, we studied in detail the amorphous phase of these semi-crystalline polymers, considering that they can present mobile (MAF) and rigid (RAF) amorphous fractions as already shown in the literature[24,25]. The MAF is made up of polymer chain segments, confined or not, which at the glass transition are mobilized. The RAF, however, is often described as being covalently linked to crystalline lamellae and this limits its mobility, so at the glass transition it remains in the glassy state. We intended to show the real effects of the RAF in rubbery materials, which might depend partly on the process used for preparing the composite films. To our knowledge, such a study has never been performed, particularly with two biopolyesters of similar chemical nature but with different degrees of crystallinity. While the crystalline phase is preponderant in PBS, the amorphous phase is the main phase in PBSA.

Polarized optical microscopy, transmission electronic microscopy, X-ray diffraction, gel permeation chromatography, flash and standard differential scanning calorimetry and rheological measurements were carried out to correlate the microstructure of the materials with their barrier properties, determined from permeation measurements made by using small diffusing molecules (gases and water) as molecular probes.

Experimental

Materials

PBS and PBSA polymers were supplied by Natureplast, France. Their chemical structure is schematized in Figure 1. The “y” group was estimated at 21 mol% by ^{1}H NMR spectroscopy. More polymer characteristics will be determined in the results and discussion sections.

Pristine sodium montmorillonite, Cloisite Na^{+} (CNa) with a CEC of 92.6 meq/100g and organo-modified montmorillonite, Cloisite 30B (C30B) with a CEC of 90 meq/100g were provided by BYK Additives, Germany. C30B is a methylbis(2-hydroxyethyl) tallow alkyl ammonium-exchanged montmorillonite clay with 25% of surfactant. C30B was chosen because of its good dispersion within PBS[26] and PBSA[27] matrices.

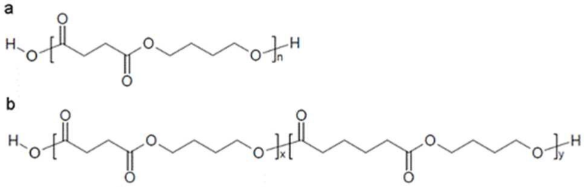

Figure 1: Chemical structure of PBS (a) and PBSA (b)

Preparation of composite films

Composites were prepared as in three steps, using the same protocol employed by Soulestin et al.[28] which was very efficient to improve the dispersion and exfoliation levels of nanoclays within PA6 matrix. Initially, polymer pellets were dried at 70 °C for 15 hours to remove residual moisture, whereas nanofillers were used as-received because Tenn et al.[29] measured better barrier properties for PLA-based films when the drying step of nanofillers was omitted. Then, the polyester pellets and 15 wt% of nanoclays were melt-mixed using a Clextral BC45 twin-screw extruder having a ratio length *L* by diameter *D* equal to 22 , with a temperature profile from 120 to 160 °C from the feed to the die. The screw speed was adjusted to 110 rpm, and polymer throughput was fixed at 10 kg.h^{-1}. At the extrusion die, the samples were cooled down in cold water and pelletized. The resulting pellets were also oven dried at 70 °C for 24 hours to avoid premature degradation.

A dilution with pure polymer by melt-mixing using a corotating twin-screw Krupp WP ZSK25 having a L/D ratio equal to 40 was performed to finally obtain samples containing 5 wt% of nanoclays. The temperature profile from the feed to the die was adjusted from 120 to 160 °C for PBS-based samples and from 120 to 180 °C for PBSA-based samples. The screw speed was fixed at 400 rpm and the throughput at 8 kg.h^{-1}. Again, the samples were cooled down in cold water and pelletized. The pellets were oven dried at 70 °C for 24 hours.

Finally, composite films were prepared from composite pellets at 5 wt% of nanoclays using two distinct methods. The first film-forming method was compression-molding, for which samples were melted for 15 minutes, at 150 °C for PBS-based composites and at 110 °C for PBSA-based composites, and a pressure of 100 bars was subsequently applied for 15 minutes. The resulting films were cooled down to room temperature. The thickness of the compressed films was adjusted to about 250 µm. The second film-forming method was the extrusion-calendering process using a Haake single screw Thermo extruder having a L/D ratio equal to 40 with a temperature profile of 120-150 °C from the feed to the die for PBS-based films and 100-135 °C for PBSA-based films. The screw speed was adjusted to 40 rpm. At the extrusion die, the samples were calendered to obtain 250 µm-thick composite films.

The samples were referenced as follows: “matrix+nanoclay(wt% of nanoclay)-**com**” for **com**pressed films and “matrix+nanoclay(wt% of nanoclay)-**ext**” for **ext**ruded-calendered films. The processes used to prepare the composite films are schematically represented in the **Figure 2**.

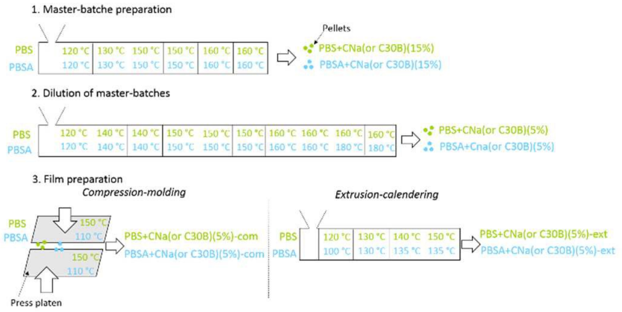

Figure 2: Schematic representation of the processes used to prepare composite films

Gel Permeation Chromatography (GPC)

The average molecular weights (Mw) of filled and unfilled films were determined with a PL-GPC 50 plus from Varian, using a PLgel 5 µm Mixed-C column, polystyrene standards for calibration, and dichloromethane as carrier solvent with a flow rate of 1 mL.min^{-1} at 27.5 °C. Previously, fillers were removed from the polymer matrix by filtration of a solution composed of the dissolved film in chloroform on a filter having 0.45 µm pore size. Results were obtained from at least two measurements performed on the film samples.

Polarized Optical Microscopy (POM)

PBS and PBSA spherulites were observed with a Leica DMLM microscope equipped with a Sony CCD camera. Each sample was placed between two glass slides and melted at 200 °C for 10 minutes. The samples were then placed in a Linkam cell and heated for 5 minutes at 150 °C. The system was finally cooled down to a temperature of 20 °C at a rate of 60 °C.min^{-1}, in order to simulate the cooling conditions used during the preparation process.

X-ray diffraction (XRD)

XRD experiments were performed on a Brucker AXS D8 Advance diffractometer using a cobalt radiation source (λ=1.789 Å) operating at 40 mA and 35 kV. The polymer matrix microstructures were studied at a diffraction angle 2ϑ ranging from 10 to 40 °, and the interlayer spacing relative to nanoclays was determined at a diffraction angle ranging from 2 to 14 °.

Transmission Electron Microscopy (TEM)

Film samples were imaged by a transmission electron microscope LEO 922 (Zeiss) with a 200 kV acceleration voltage to show the levels of nanoclay exfoliation and dispersion (highlighting large aggregates up to isolated and well-dispersed clay platelets). The samples were cut with a Reichert cryo-microtome (-30 °C for the sample and -40 °C for the knife): ultrathin sections approximately 95 nm thick were cut using a cryo-diamond knife with a cup angle of 35 ° (Diatome, Switzerland) and transferred to 400 mesh copper grids.

Melt Rheology

Melt rheological measurements were carried out in oscillatory mode using a Haake Mars rheometer III equipped with a 35 mm diameter cone-plate. Measurements were performed at 140 °C under nitrogen flux to avoid polymer chain degradation. The linear viscoelastic domain relative to each sample was previously determined using an angular frequency of 100 rad.s^{-1}.

Differential Scanning Calorimetry (DSC)

DSC experiments were carried out with a TA Instrument DSC-Q100 apparatus under nitrogen atmosphere. Each 5-10 mg film encapsulated in a standard DSC aluminum alloy pan was heated from -60 °C to 150 °C at a rate of 10 °C.min^{-1} and then cooled down to -60 °C at the same rate. The melting and crystallization temperatures were determined from the curves obtained from the heating step and the cooling step, respectively. The degree of crystallinity was calculated from the first heating step using the following equation:

$$Xc(\%) = 100 \cdot \frac{\Delta Hm - \Delta H_{cc}}{\Delta H_m^0 \cdot (1 - W_f)}$$ **Equation 1**

where ΔHm is the melting enthalpy, ΔH_{cc} is the cold crystallization enthalpy, ΔH_m^0 is the melting enthalpy of a 100% crystalline PBS equal to 110.3 J.g^{-1} [30] and W_f is the wt% of the fillers.

Usually the second heating step is used to remove the thermal history of the material. In our case, the material structure was analyzed from the first heating step as it is supposed to be during the permeation measurements.

Flash Differential Scanning Calorimetry (Flash-DSC)

The mobility of macromolecular chains in unfilled films and composite films was evaluated with Flash DSC. Experiments were carried out using a Flash DSC 1 twin-type power-condensation fast scanning chip calorimeter provided by Mettler-Toledo. A Hubert TC100 intracooler was used to cool down samples to 178 K with a very high cooling rate. A 20 mL.min^{-1} flow rate of nitrogen was used to avoid water condensation from the environment. A film sample was placed on a MultiSTAR UFS 1 MEMS chip sensor. To evaluate the sample mass, an identical protocol was applied on the film introduced in the Flash-DSC and on another film placed on the Q100 DSC[31]. First, the thermal history of the films was removed by a heat step at 150 °C for 60 s. Then, they were cooled down for 600 s to their crystallization temperature, previously determined on the standard DSC, in order to crystallize the materials as much as possible. Finally, the sample masses were estimated by comparing the melt enthalpy measured from the second heat step on the two DSC curves.

As a result, the masses were estimated at 83 ± 8 nanograms for the PBS film and at 247 ± 25 nanograms for the PBSA film. The rigid amorphous fraction, X_{ra}, was determined by:

$$X_{ra}(\%) = 1 - (X_c + X_{ma})$$ **Equation 2**

where X_c is the crystallinity degree and X_{ma} is the mobile amorphous phase fraction. X_c was calculated using Equation 1 and X_{ma} is deduced from Equation 3.

$$X_{ma}(\%) = \frac{\Delta Cp}{\Delta Cp^0}$$ **Equation 3**

where ΔCp is the specific heat capacity at constant pressure for the unfilled polymer, determined by classical DSC from the first heating step, and ΔCp^0 is the specific heat capacity at constant pressure for a 100% amorphous polymer determined by Flash-DSC

PBS and PBSA samples were first melted at 150 °C for 60 s, and then cooled down to -90 °C at 1000 °C.s^{-1} and re-heated to 150 °C at 1000 °C.s^{-1}. ΔCp^0 of PBS and PBSA polymers were determined from the second heating step, and in this case the polymers were 100% amorphous.

Gas permeation

Gas permeation measurements were performed at 25 °C by using a barometric method known as "Time-lag" permeation. The film tested was placed in a measurement cell composed of two compartments (the upstream and downstream sides), as described by Joly et al[32]. Briefly, the measurement cell was initially purged for 15 hours. Then, the carrier gas (N_2, O_2, or CO_2) was introduced into the upstream side of the cell. In the downstream side, the increase of pressure was recorded over time using a pressure sensor, which allows the quantity of diffusing molecules per surface unit to be determined. The flux *J* as a function of time was also plotted. At the stationary state of the flux curve, the flux *J* remains practically constant ($J = J_{st}$) and the permeability coefficient *P* (expressed in Barrer units) was calculated by:

$$P = \frac{J_{st} \cdot \delta}{\Delta p} \qquad \textbf{Equation 4}$$

where J_{st} is the flux at the stationary state, δ is the film thickness and Δp is the pressure difference between the upstream and downstream sides of the measurement cell.

By assuming no plasticization effect is induced by the diffusing gas molecules, the diffusion coefficient *D* can be calculated as follows:

$$D = \frac{\delta^2}{6.t_l} \qquad \textbf{Equation 5}$$

where t_l represents the time called "time-lag" which was determined from the intercept of the asymptotic straight line of the stationary flux with the time axis.

The solubility coefficient *S* of diffusing gas molecules in the film can be obtained by:

$$S = \frac{P}{D} \qquad \textbf{Equation 6}$$

Each measurement was done at least twice.

Water permeation

Water permeation measurements were carried out at 25 °C with a home-made permea-diffusiometer composed of two main devices: a chilled mirror hygrometric detector (General Eastern Instruments, Massachussetts, USA), and a permeation cell made of two compartments (the upstream and downstream sides) separated by the film tested. A complete description has been given by Alexandre et al.[23].

First, dry nitrogen flow was injected into the measurement cell to dry the film until a constant dew point temperature above -70 °C was reached. Distilled liquid water was then introduced through the upstream side of the cell, and the water concentration in the downstream side was determined as a function of time *t* using the hygrometric detector. The water flux curve thus obtained $J = f(t)$ is usually described by three successive periods. During the first period, as the water molecules have not reached the downstream side of cell, the water flux is nil. Then, when the first molecules have passed through the tested film, the J value progressively increases. This period is called the transient state. When the water flux becomes constant, the stationary state of the permeation is also reached and the *J* value is equal to J_{st}. The permeability coefficient P (expressed in Barrer units) is directly proportional to J_{st} and given by:

$$P = \frac{J_{st} \cdot \delta}{\Delta a} \qquad \textbf{Equation 7}$$

where J_{st} is the flux at the stationary state **,** δ is the film thickness and Δa is the difference in water activity (driving force) between the upstream and the downstream sides of the measurement cell. The water activity in the upstream side is considered approximately equal to 0, so that $\Delta a = 1$.

Diffusion coefficients were determined from the slope of the water flux curve during the transient state. By solving Fick's diffusion equations, a dimensionless flux curve as a function of a reduced time $j = f(\tau)$ is plotted; where $j = \frac{J}{J_{st}}$ and $\tau = \frac{D \cdot t}{\delta^2}$. D is the diffusion coefficient, which is assumed to be constant, and t is the measurement time.

In order to discover whether or not the diffusion coefficient depends on the permeant concentration, D was calculated at two characteristic points of the permeation curve, the inflexion point *I* and the time-lag point *L*[33]. From the theoretical dimensionless flux curve, considering D as a constant, these two characteristic points were determined as follows:

$$j_I = J(\tau_I) = 0.24 \qquad \textbf{Equation 8}; \qquad j_L = J(\tau_L) = 0.62 \qquad \textbf{Equation 9}$$

$$\tau_I = 0.09104 = \frac{D_I \cdot t_I}{\delta^2} \qquad \textbf{Equation 10}; \qquad \tau_L = \frac{1}{6} = \frac{D_L \cdot t_L}{\delta^2} \qquad \textbf{Equation 11}$$

The experimental times noted $t_{0.24}$ and $t_{0.62}$ corresponding to $j_{0.24}$ and $j_{0.62}$, respectively, were determined from the curve $j = f(t)$. The coefficients $D_{0.24}$ and $D_{0.62}$, also called D_I and D_L, were then calculated and compared. A difference in values highlights the water concentration-dependence of the diffusion. In the case of vapor permeants, it is usually observed that D increases with an increase in the permeant concentration. Such behavior is attributed to a plasticization phenomenon induced by the diffusing species, which leads to an increased free volume. This well-known behavior, considered as a Fickian process of type B[34], is usually fitted to an exponential law of diffusion according to:

$$D = D_0 e^{\gamma \cdot C} \qquad \textbf{Equation 12}$$

where D_0 is the diffusion coefficient when the permeant concentration is close to 0, γ is the plasticization factor and C is the local concentration of the permeant molecules.

From the curves obtained, it is possible to determine the mean integral diffusion coefficient *<D>* as follows:

$$< D >= \frac{1}{\Delta C} \int_{C_1}^{C_2} D(C).dC \qquad \textbf{Equation 13}$$

where C_1 and C_2 are the water concentrations in the boundary conditions at the upstream and downstream sides of the film, respectively. From this equation, it is possible to determine the maximum coefficient diffusion D_M, which corresponds to the coefficient diffusion at the stationary state:

$$D_M = D_0 . e^{\gamma . C_{eq}} \qquad \textbf{Equation 14}$$

where *Ceq* is the water concentration in the film at the stationary state.

Each measurement was carried out at least twice.

Results and discussions

Structural characterization

Composite properties are known to be highly dependent on the composition and microstructure of a composite. Therefore, it is essential to characterize the polymer structure, and the dispersion and exfoliation levels of nanofillers in composite films.

Film preparation requires several steps, so the polymer chain degradation can occur at any point. The average molecular weights of the polymers were thus calculated before and after the film preparation by means of GPC measurements, and the values are gathered in Table 1.

Table 1 : Molecular weights of the elaborated films

*Mw**10^{-5} (g.mol^{-1})	Commercial pellets	Compression-molding	Extrusion-calendaring
PBS	1.39 ± 0.01	1.39 ± 0.02	1.26 ± 0.06
PBS+CNa(5%)	/	1.36 ± 0.03	1.33 ± 0.06
PBS+C30B(5%)	/	1.02 ± 0.01	1.05 ± 0.07
PBSA	1.84 ± 0.02	1.78 ± 0.01	1.49 ± 0.11
PBSA+CNa(5%)	/	1.54 ± 0.01	1.40 ± 0.10
PBSA+C30B(5%)	/	1.31 ± 0.01	1.18 ± 0.10

Table 1 shows that the molecular weight of the PBSA pellets is higher than that of the PBS pellets. In addition, higher *Mw* values are obtained for the compressed films compared to the extruded-calendered films. This result indicates that the extrusion-calendering process exerts a more degrading effect than the compression-molding process. This can be explained by the higher shear rate applied during the extrusion-calendering process, which, through a chain scission mechanism, contributes to greater degradation of the polymer chains[35]. The values in Table 1 also show that the differences in the reduced *Mw* between the extrusion-calendering and the compression-molding processes are more pronounced for PBSA-based films than for PBS-based films. This finding is probably due to the higher *Mw* of the PBSA.

Concerning the composite films, the incorporation of CNa has only a slight impact on the *Mw* of our polymers, while the incorporation of C30B leads to a decrease in the *Mw*. This well-known phenomenon is attributed to the degradation of the C30B surfactant occurring during film preparation due to the high processing temperature, as the thermal stability of C30B is lower than that of CNa[15]. The resulting degradation products can randomly promote a hydrolysis reaction on the polymer chains[36]. Nevertheless, on the basis of the values gathered in Table 1, the decrease in the *Mw* values of the two polyesters (up to 25% for PBS and 35% for PBSA) is probably not sufficient to negatively impact barrier properties, as recently mentioned in the literature[29].

Since PBS and PBSA polyesters are semi-crystalline polymers, the structure composed of crystalline and amorphous phases was investigated by X-ray diffraction at a 2θ diffraction angle range of 10-40 ° (Figure 3), and by DSC (Figure 4). It is worth pointing out that changes in structure and in crystallinity could affect the barrier performances; the crystalline phase of a polymer acts as an obstacle to the diffusion of small molecules (permeants), that only occurs in the amorphous phase.

X-ray diffraction was performed on the surfaces and the cross sections of each film, in order to calculate the degree of crystallinity, and to indicate whether the different directions of analysis highlighted different degrees of crystallinity, thus showing texture effects.

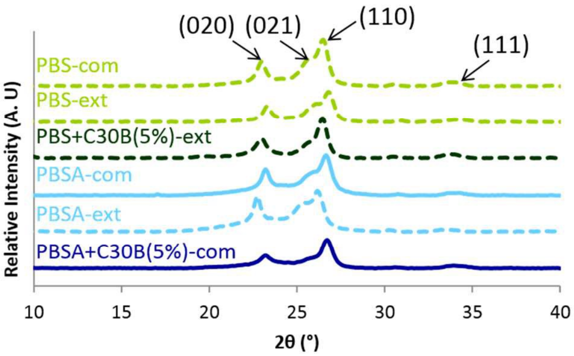

Figure 3 : X-ray diffraction spectra of PBS-based films and PBSA-based films

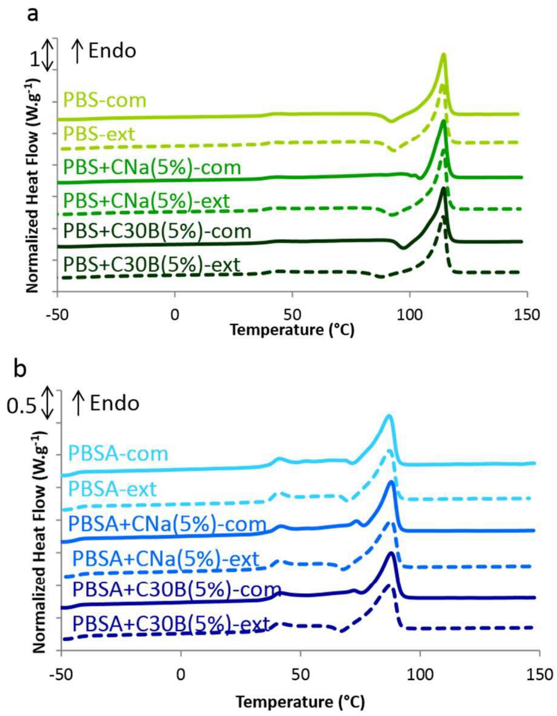

Figure 4 : DSC curves of PBS-based films (a) and PBSA-based films (b)

X-ray diffraction carried out on the films' surfaces (Figure 3) reveal that the unfilled PBS and PBSA films exhibit an amorphous halo centered on 2θ = 24 ° and four strong diffraction peaks located at 22.9, 25.7, 26.5 and 33.5 °. It has been reported in the literature that PBS and PBSA polyesters crystallize in a monoclinic crystal lattice. The lattice parameters being well-determined, the diffraction peaks can be attributed to (020), (021), (110) and (111) planes[37,38], respectively. The crystallinity degree of the films (noted *Xc, XRD, surface*) was determined from the deconvolution of amorphous and crystalline contributions. Whatever the direction of analysis, the PBS composite films have a higher crystallinity degree, than the PBSA composite films, with values close to those of the unfilled films. The XRD spectra of all our composite films also appear very similar to those of the unfilled films.

Likewise, the DSC curve shapes for all the films (Figure 4) are practically similar. Indeed, the DSC curves from the low to the high temperatures show the same thermal transitions: the glass transition with a small heat capacity step, the melting of small and imperfect crystals ($T \approx 40$ °C), a cold crystallization before all the remaining crystals melt, as already observed by Makhatha et al.[7]. For each composite (based on either PBS or PBSA), after allowing for measurement errors, the glass transition, the cold crystallization and the melting temperatures are considered to be very close. It seems, therefore, that the polymer microstructure is not significantly affected by the incorporation of nanoclays, whatever the preparation process. The glass transition temperatures (*Tg*), heat capacity steps (*ΔCp*), apparent melting temperatures (*Tm*), crystallization temperatures (*Tc*) and crystallinity degrees (*Xc*) are reported in Table 2.

Table 2 : Glass transition temperature (*Tg*), specific heat capacity (*ΔCp*), apparent melting temperature (*Tm*), crystallization temperature (*Tc*) and crystallinity degree (*Xc*) determined by DSC (noted *Xc, DSC*), *Xc* determined by XRD of film surface (noted *Xc, XRD, surface*) and *Xc* determined by XRD of film cross section (noted *Xc, XRD, cross section*).

	Tg (°C)	*ΔCp* ($J.g^{-1}.K^{-1}$)	*Tm* (°C)	*Tc* (°C)	*Xc, DSC** (%)	*Xc, XRD*, surface* (%)	*Xc, XRD*, cross section* (%)
PBS-com	-32.5	0.07	114.4	78.0	63	76	58
PBS-ext	-33.2	0.14	114.4	77.8	58	75	57
PBS+CNa(5%)-com	-32.5	0.06	114.4	90.6	62	70	60
PBS+CNa(5%)-ext	-33.2	0.11	114.6	91.5	58	70	60
PBS+C30B(5%)-com	-31.3	0.11	114.5	88.5	55	72	60
PBS+C30B(5%)-ext	-33.1	0.12	114.2	89.1	61	76	56
PBSA-com	-44.2	0.28	87.2	36.9	36	61	46
PBSA-ext	-43.6	0.23	87.2	59.2	41	55	46
PBSA+CNa(5%)-com	-43.9	0.26	87.8	51.7	38	61	43
PBSA+CNa(5%)-ext	-43.1	0.23	87.7	55.2	40	61	44
PBSA+C30B(5%)-com	-44.2	0.23	87.9	47.2	38	61	44
PBSA+C30B(5%)-ext	-43.6	0.20	87.5	47.4	39	63	42

* Accuracy = ± 3

XRD and DSC both show higher crystallinity degrees for PBS-based films than for PBSA-based films. Furthermore, as PBS and PBSA crystallize in a monoclinic crystal lattice, the higher melting temperature measured for the PBS films indicates larger sizes of crystalline lamellae within these films, compared with the PBSA films.

Whatever the film tested, the degrees of crystallinity calculated from XRD spectra on the film surface were found to be higher than those determined from DSC curves (Table 2). Such a discrepancy has already been reported in the literature for nylon samples[39] and for PA12-based composite films[23]. However, the degrees of crystallinity calculated from XRD on the cross sections were closer to the DSC results (the difference is lower than 5 % for most of the samples). This finding, highlights the relevance of our approach which uses both analytical techniques (XRD and DSC). Indeed, the crystallinity degree calculated from XRD depends on the crystal orientation[40], which is not the case for DSC. XRD measurements from two film orientations could also show whether a texture exists in the sample. To determine an average crystallinity degree independently of the direction of the beam, radial intensity profiles, *I(2ϑ)* and azimuthal integration are usually used[25]. Therefore, in our case, the difference in degree of crystallinity between the surface and the cross section of the films analyzed reveals a crystal texture.

The organization of these crystals in spherulites can be observed on POM images. Figure 5 shows a larger average spherulite size for the PBS-based films (diameter of about 40 µm) compared with the PBSA-based films (diameter of about 15 µm). Moreover, PBS is much more birefringent than PBSA, probably due to the higher number of crystals in PBS compared to PBSA. In addition, unlike the PBS spherulites, the PBSA spherulites are ringed. In fact, the “y” group in the chemical structure of the PBSA copolymer (Figure 1) acts as an impurity and hinders the crystallization of the “x” group[41]. Consequently, during crystallization, lamella growth continues up to the vicinity of a non-crystallizable “y” group, creating a torsion zone. After that, the lamella-growing phenomenon proceeds with a small derivation angle. This behavior has already been observed in other copolymers such as poly[(3-hydroxybutyrate)-co-(3-hydroxyhexanoate)][42], and poly(3-hydroxybutyrate-co-3-bydroxyvalerate)[43].

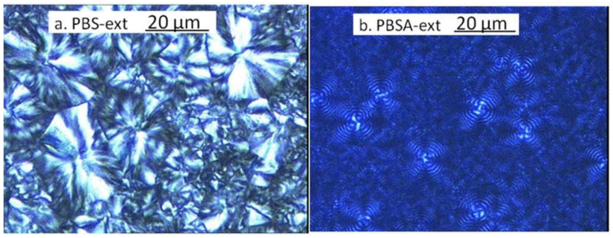

Figure 5 : POM observation of PBS-ext (a) and PBSA-ext (b) neat films.

From POM images, a statistical study of the spherulite size was carried out for all the composite films to evaluate size distribution in the film. More than 100 spherulites were measured in 7 to 10 images per sample in order to determine the crystal diameter (Figure 6).

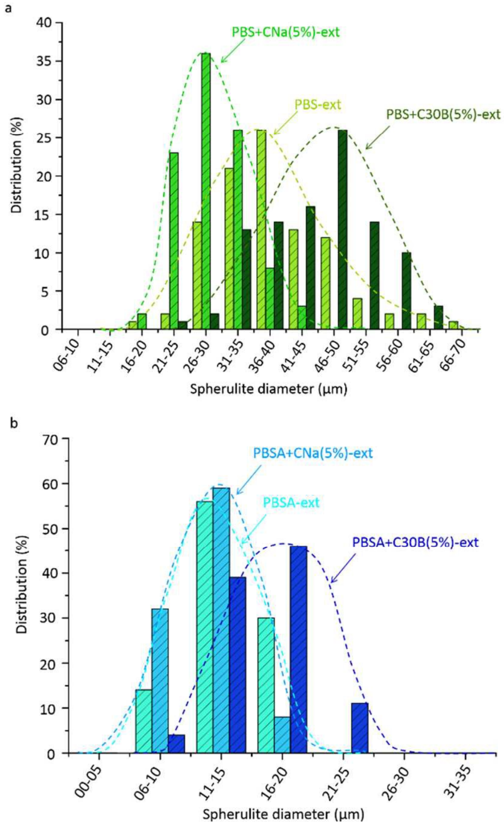

Figure 6 : Distribution of spherulite size in the compressed extruded-calendared PBS-based film (a), extruded-calendared PBSA-based films (b).

Spherulite size distribution for the extruded-calendered and the compressed films (data not shown here) seems to be very similar, irrespective of the polyester matrix. However, this observation needs to be somewhat qualified because of the thermal treatment applied to the samples to erase their thermal history. Nevertheless, it is clearly evidenced that the incorporation of native or organo-modified montmorillonites affects the mean spherulite diameters in the PBS-based and the PBSA-based films (Figure 6). In the PBS-based films, the introduction of CNa reduces the mean spherulite diameter. This observation can be related to well-known nucleating effects generated by nanoclays in polymer matrices[44]. In fact, clay-induced nucleating effects are usually highlighted when a higher crystallization temperature for composite films is obtained compared to the neat matrix. With the nanoclay-induced nucleating effects, spherulites collide with each other during growth, and this limits their size. Moreover, as mentioned earlier, the incorporation of CNa in PBS creates clay aggregates because of the incompatibility between the highly hydrophile inorganic fillers and the hydrophobic organic matrices. The same behavior has already been observed by Strawhecker et al.[45] who have shown that CNa aggregates could hinder the spherulite growth of poly(ethylene oxide) and so reduce the size. Regarding the PBSA-based films, no significant change in spherulite size is observed with the incorporation of CNa. Indeed, the crystallization of PBSA is hindered by the presence of the “y” group as demonstrated with the lower crystallization temperature of PBSA-based films compared to the PBS-based films. The negligible effect of the presence of CNa on the spherulite sizes in PBSA films can be attributed to the fact that the PBSA spherulites and their crystalline lamellae are already small compared to those of PBS, with the fillers being more dispersed in the larger PBSA amorphous fraction.

When C30B is incorporated, however, the spherulite sizes increase in both PBS and PBSA matrices. This result has already been reported by Ray et al.[46] for PBSA-based systems and the authors have pointed out fewer nucleating effects for C30B than for CNa. Indeed, the authors have found that crystallization temperatures for C30B/composite films are lower than for CNa/composite films. Ray et al.[46] have also demonstrated that the crystallization kinetics of PBSA is very slow in the presence of C30B. So, the weaker nucleating effects of C30B and the slower crystallization kinetics of PBSA led to larger spherulites forming than when CNa was introduced. Usually, the properties of semi-crystalline polymers are evaluated on the basis of a system composed of two phases: a crystalline phase and an amorphous phase. However, it has already been shown that two distinct, but adjacent, amorphous fractions can coexist within a material[47,48]. The first one is the Mobile Amorphous Fraction (MAF) where the polymer chains are free to move when the polymer is in the rubbery state. The second one is the Rigid Amorphous Fraction (RAF) resulting from the mobility of the polymer chains, which is strongly hindered in the vicinity of crystals and/or nanoclays. Kuwabara et al.[49] have evidenced the existence of an intermediate phase between the crystal and amorphous phases by means of solid state ^{13}C NMR measurements for both PBS and PBSA samples. The RAF is somewhat difficult to be clearly defined, however it can be considered as amorphous segments of restricted mobility and located in interlamellar and interfibrillar regions. Besides, even if MAF refers rather to the interspherulitic regions, the RAF can also occur in these regions and especially at the vicinity of the dispersed and exfoliated nanoclays which induce a local stiffness. This last consideration would be consistent with the increase of RAF after adding C30B nanoclays in PBSA. There is not a clearcut transition between RAF and MAF but rather a distribution between these extreme cases. To calculate the MAF and RAF in the PBS-based and PBSA-based films, the specific heat capacity of the 100 % amorphous unfilled polymers (noted ΔCp^0) must be known. As a cooling step using standard DSC is not sufficient to amorphize PBS and PBSA polyesters, it was necessary to turn to a specific and appropriate technique such as the Flash-DSC technique, which is able to cool down samples at a very high rate. Bandyopadhyay et al.[50] have characterized the MAF of PBSA nanocomposites containing C30B by using a high speed differential scanning calorimetry. From the determination of *ΔCp* for semicrystalline and amorphous PBSA, they calculated the MAF of PBSA which was equal to 61.1%. Also considering their results of enthalpies of cold crystallization and of fusion and assuming the melting enthalpy of a 100% crystalline PBSA equal to 110.3 J.g^{-1}, the crystallinity degree of their PBSA can be estimated to 36%, that is the same result for our PBSA-com films (Table 2). From that, the RAF of their PBSA can be deduced and is equal to 2.9%. In our case, in order to obtain 100 % amorphous materials, the adequate cooling rate to completely prevent crystallization, was determined. Thus, the sample was heated for 60s at 150 °C. The melted polymer was then cooled down to -90 °C using several cooling rates (from 1000 to 0.01 °C.s^{-1}). In order to determine if the cooling rate was sufficient to amorphize the polymer, the sample was re-heated at 1000 °C.s^{-1} from -90 to 150 °C. Data were recorded from this last step and the corresponding curves are plotted in Figure 7. The absence of an endothermic peak reveals that the material is completely amorphous.

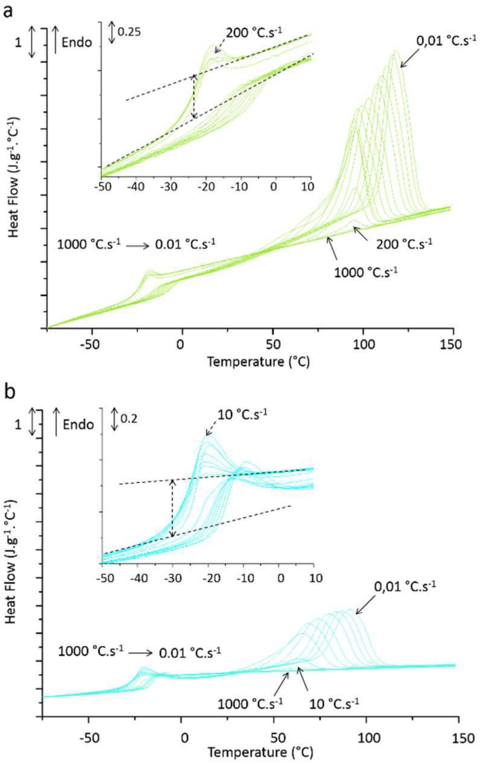

Figure 7 : DSC curves obtained for several cooling rates (from 1000 to 0.01 °C.s^{-1}) for (a) PBS and (b) PBSA

It was found that to obtain 100 % amorphous polymers the adequate cooling rate must be higher than 200 °C.s^{-1} for the unfilled PBS film and higher than 10 °C.s^{-1} for the unfilled PBSA film. The inserts in the figures show clearly two families of glass transition phenomena: the glass transition of wholly amorphous materials with a weak endothermic peak due to the thermal protocol, and the glass transition of semi-crystalline materials. The latter is, as usual, very broad when the crystallinity degree is high[51] (here for PBS).Therefore, to ensure that no crystallization occurs, a cooling rate of 1000 °C.s^{-1} was used, allowing the specific heat capacity *ΔCp⁰* of both the 100 % amorphous polyesters to be determined. From Flash-DSC curves, the determined *ΔCp⁰* values were 0.51 J.g^{-1}.°C^{-1} for PBS and 0.43 J.g^{-1}.°C^{-1} for PBSA. In the study of Bandyopdhyay et al.[50], the *ΔCp⁰* of PBSA measured at a heating rate of 200 °C.min^{-1}, after a cooling carried out at 1000 °C.min^{-1}, was 0.614 J.g^{-1}.°C^{-1}. This higher value compared to our can be explained by the presence of a chain extender (0.5 mol%) in PBSA. Due to an uncertainty of the sample masses (the values being very low), the accuracy of the values can be estimated with a measurement error of 10 %.

The RAF should normally be calculated by determining the glass heat capacity and the liquid heat capacity at different temperatures, using advanced thermal analysis (temperature-modulated differential scanning calorimeter (TM-DSC), quasi isothermal DSC). In this work, however, the RAF in the films was calculated at the glass transition temperature, -25 °C, of amorphous PBS and PBSA, while permeation experiments were carried out at 25 °C. TM-DSC was not used because the heating rate is so slow that both PBS and PBSA samples would have rapidly crystallized and it would have been impossible to evaluate their RAF at 25 °C. The RAF must decrease slightly after the glass transition temperature as already reported by Riggheti et al.[52] in poly(ethylene terephthalate), where a small decrease of about 8 % between the end of the glass transition and *Tg* + 50 °C was noted, a decrease that will be the same for all the composite films with the same polymer matrix, so the correlation between the RAF and the barrier properties investigated at 25 °C will still be relevant.

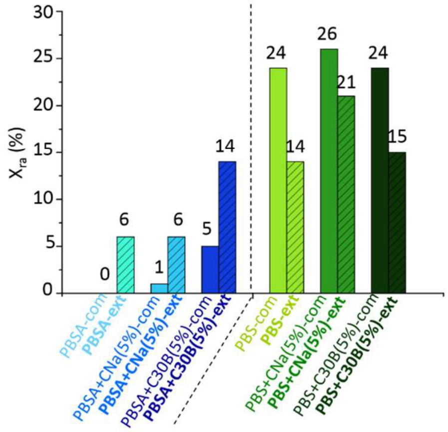

Figure 8 : Rigid amorphous fraction of PBS-based films and PBSA-based films

The rigid amorphous fractions, noted X_{ra}, were calculated from the *ΔCp⁰* values (Figure 8). It is interesting to note that the X_{ra} value (3%) found for the PBSA studied by Bandyopadhyay et al.[50] is the intermediate value between those of PBSA-com and PBSA-ext and that is consistent with our results. A higher RAF was obtained in the PBS-based films than in the PBSA-based films. As PBS is more crystalline than PBSA, more crystal-amorphous interfaces probably exist and the amorphous phase is, as a result, more constricted between the crystalline phases than for PBSA. The preparation process induced different effects in the films. Compression-molding favored the formation of RAF in the PBS-based films more than extrusion-calendering, while for the PBSA-based films, the opposite was observed. In their study, Bandyopadhyay et al.[50] show how MAF is related to the degree of dispersion of C30B in PBSA and hence final properties. Indeed, as expected, the lowest MAF (highest RAF) was obtained for the nanocomposite of highly dispersed silicate layers. Analogously with our PBSA, the highest RAF obtained with PBSA+C30B(5%)-ext can be related to the highest degree of dispersion of C30B in PBSA.

Evaluation of dispersion and exfoliation levels of nanoclays within the matrix

The dispersion and exfoliation levels of the nanoclays in the composite films were first evaluated by means of XRD experiments using a 2θ diffraction angle range from 2 to 14 ° (Figure 9) in accordance with the diffraction patterns for montmorillonite.

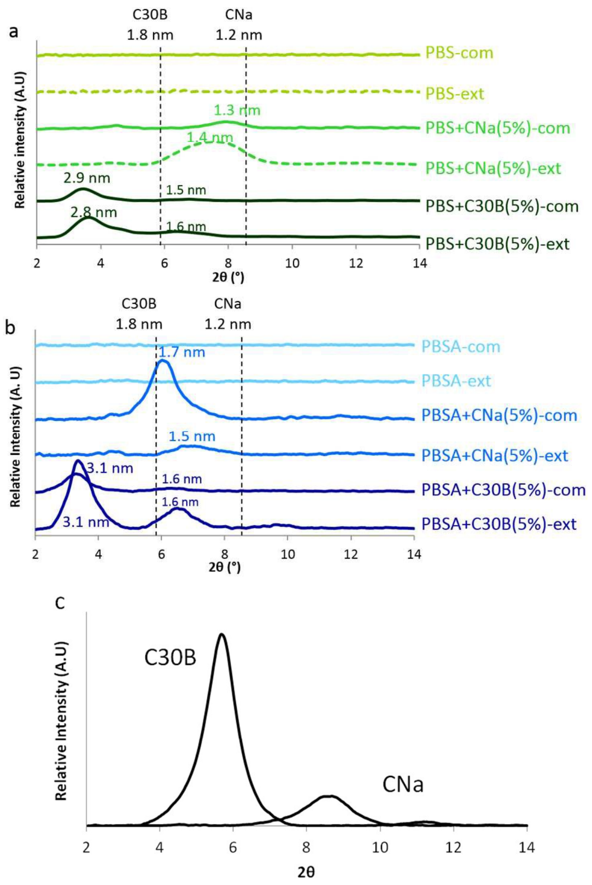

Figure 9 : XRD spectra of the PBS-based films (a), the PBSA-based films (b) and nanofillers (c).

Before all measurements, the CNa and C30B powder patterns were determined (Figure 9). In agreement with the literature, only one diffraction peak per nanoclay was observed, corresponding to an interlayer distance of 1.2 nm for CNa[12] and 1.8 nm for C30B[46]. At the same diffraction range, no diffraction peak was observed in the XRD spectra of the unfilled polymer films, whatever the preparation process. One can infer that the diffraction peak observed in the XRD spectra of the composite films is only associated to the diffraction of the clays. As expected, the interlayer spacings related to the nanoclays are higher for the C30B/composites than for the CNa/composites.

CNa aggregates are still present in materials containing CNa, despite the interlayer distances being slightly increased by both preparation processes. The higher interlayer distances found in the films containing C30B, indicated the formation of intercalated structures. Finally, it seems that applying either extrusion-calendering or compression-molding does not significantly affect the clay interlayer distance.

TEM is usually used as an additional support to evaluate the quality of nanoclay dispersion and exfoliation (Figure 10).

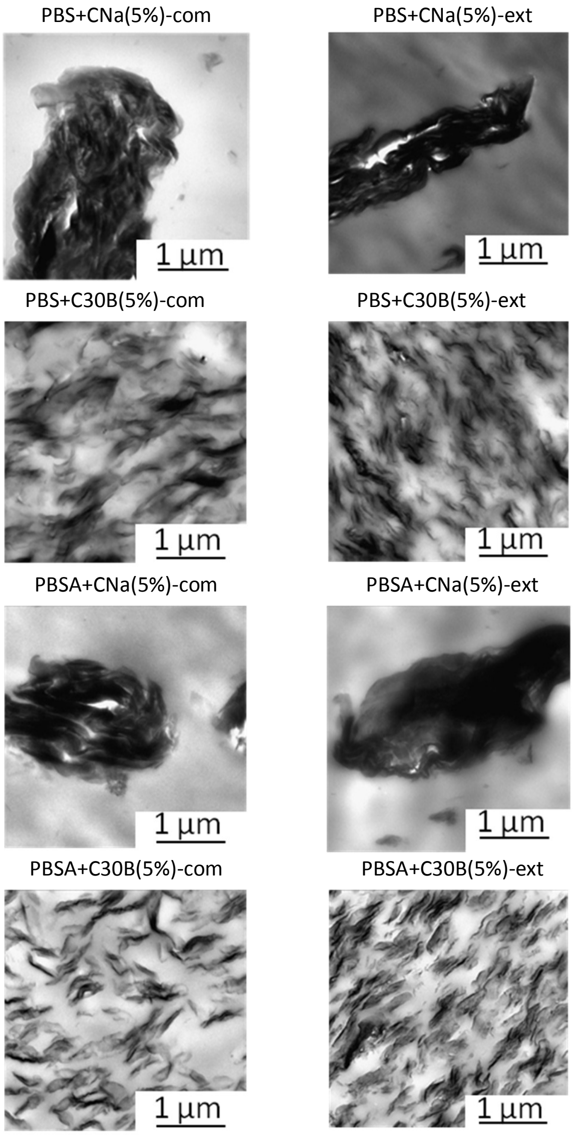
PBS+CNa(5%)-com PBS+CNa(5%)-ext
PBS+C30B(5%)-com PBS+C30B(5%)-ext
PBSA+CNa(5%)-com PBSA+CNa(5%)-ext
PBSA+C30B(5%)-com PBSA+C30B(5%)-ext

Figure 10 : TEM images of composite films

The TEM observations are in good agreement with the XRD results. Indeed, whatever the matrix, while aggregated structures clearly resulted from incorporating CNa, intercalated and exfoliated structures were obtained in the case of C30B (Figure 10). This finding can be related to organo-modification which favors the intercalation of polymer chains in nanoclay platelets. Intercalated structures are mainly obtained in compressed films, while individualized platelets coexist with intercalated structures in extruded-calendered films. This observation clearly suggests a higher exfoliation level of C30B in both PBS and PBSA matrices with extrusion-calendering, compared with compression molding. The exfoliation level seems to be even higher in the case of PBSA-based films. In addition, due to shear forces, an alignment of platelets was obtained in the extrusion flow direction.

In addition to TEM observations and XRD measurements, dynamic rheological measurements were carried out as a complementary tool to evaluate clay exfoliation and dispersion levels. It is generally accepted that complex viscosity at low frequencies is correlated to clay exfoliation levels[53], better exfoliation leading to significantly increased viscosity. This increase is commonly assigned to the formation of a nanoparticle network (composed of small tactoids or exfoliated clay platelets), which is only observed when the nanoparticles are finely exfoliated in the polymer matrix. If exfoliation occurs, a transition from liquid-like to solid-like behavior is observed, even at low nanofiller content. Figure 11 shows the evolution of the complex viscosity η^* as a function of angular frequency for the PBS-based and PBSA-based films.

For the unfilled films, the preparation processes impacted on the complex viscosity. Extrusion-calendering resulted in lower η^* values than compression-molding, especially for the unfilled PBSA films, meaning that extrusion-calendering degraded the polymer chains more than compression-molding, as also revealed by GPC measurements (Table 1).

For the composite films, the flow properties were totally different depending on the nature of the clay. In the case of CNa, the rheological properties at low frequencies, characteristic of materials without exfoliation structures, were similar for both matrices. These rheological results confirm the absence of CNa exfoliation due to the limited interactions between clays and matrix. This is in good agreement with TEM observations, which show clay aggregate formation in our hydrophobic polymers (PBS and PBSA). In addition, it can be noted that the complex viscosity of CNa/composites decreases, compared to the unfilled film values. This means that native clay contributes to the degradation of both matrices, but to a greater extent in PBSA. Again, these results are also consistent with GPC measurements. Finally, by incorporating CNa into PBS and PBSA, the resulting materials are microcomposites rather than nanocomposites. In the case of C30B, the rheological behavior of the resulting composites is totally different; the complex viscosity is significantly increased at low frequencies. In this specific region, a transition from liquid-like to solid-like rheological behavior was observed, which demonstrates that the C30B platelets were well-exfoliated in PBS and PBSA. Moreover, considering the complex viscosity versus frequency, the results tend to show that the exfoliation level is improved in the case of the extruded films compared to the compressed films, whatever the matrix.

To explore in more detail the level of exfoliation, the complex viscosity versus frequency curves were fitted using a modified Carreau-Yasuda law (with a yield stress). Recent works[54,55] recommend this model as a relevant model to accurately estimate the level of clay exfoliation. It is admitted that the apparent yield stress (σ_0) is directly correlated to the physical interactions existing between clay particles, which increases as the fraction of exfoliated platelets increase. At the same clay content, the yield stress value is influenced only by the exfoliation level. The apparent yield stress can be determined by fitting the complex viscosity data with the Carreau-Yasuda law including an additional term of yield stress σ_0/ω (ω is the angular frequency, η_0 is the zero-shear viscosity, λ is the average relaxation time, *n* is the flow index and *a* is the curvature parameter) (Equation 15).

$$|\eta^*(\omega)| = \frac{\sigma_0}{\omega} + \eta_0[1 + (\lambda\omega)^a]^{(n-1)/a} \qquad \textbf{Equation 15}$$

Table 3 gathers values of apparent yield stresses for all the films. No apparent yield stress is observed for the unfilled films. For microcomposite films, i.e. films containing CNa, the apparent yield stress equal to 0 confirms that the exfoliation of CNa in PBS and PBSA matrices was very limited, as previously discussed. In the case of C30B, all the composite films, defined as nanocomposite, were characterized by an apparent yield stress due to the presence of exfoliated clay particles of high aspect ratio. The comparison between the extruded-calendered and the compressed films clearly shows that the exfoliation is improved in the case of the extruded-calendered films. The high shear rate induced during extrusion-calendering clearly improved nanoclay exfoliation levels.

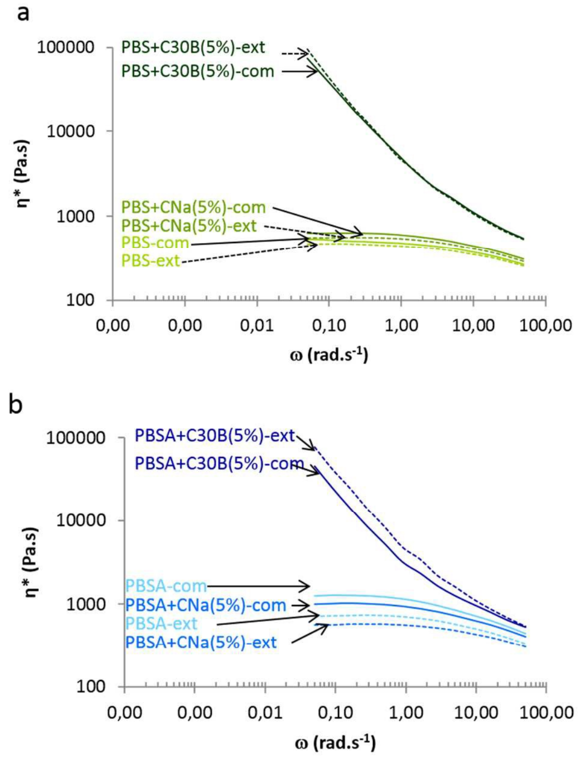

Figure 11 : Complex viscosity of the PBS-based-films (a) and the PBSA-based films (b)

Table 3 : Apparent Yields stress values of the PBS-based and PBSA-based samples

	PBS-com	PBS-ext	PBSA-com	PBSA-ext
Unfilled	0	0	0	0
CNa	0	0	0	0
C30B	693	902	433	733

To conclude, the combination of TEM observations, XRD measurements and rheological analyses helped to evaluate the exfoliation and dispersion levels of nanofillers in polyester matrices.

While TEM images showed high C30B clays orientation in PBS-based and PBSA-based films prepared with the extrusion-calendering process, XRD experiments revealed the absence of significant effects of the preparation processes on intercalated structures, and finally rheological analyses quantitatively determined higher clay exfoliation levels in the extruded-calendered films than in the compressed films.

Evaluation of barrier properties of elaborated composite films

Gas transport properties

The permeation through a polymer film mainly depends on the structure of the film, and on the dynamic diameter φ_d and the critical temperature T_{cr} of the diffusing molecules. In most cases, molecules with a small dynamic diameter diffuse more easily than larger molecules, so the permeability increases, even though, with their low critical temperature, the solubility of these diffusing molecules is reduced.

So, three gas molecules (N_2, CO_2 and O_2), differing in dynamic diameter and critical temperature, were selected to investigate the barrier properties of our composite films in order to show how the behavior of the polyester matrix is affected by the presence of the nanoclays and by the process used in preparing the film.

In the present study, all the films showed the same tendency; $P(N_2) < P(O_2) < P(CO_2)$ (Figure 12), as reported by Van Krevelen[56]. This can be explained as follows: the higher critical temperature of CO_2 (31.15 °C) compared to that of N_2 (-146.94 °C) and that of O_2 (-118.56 °C)[57] leads to a greater permeability to carbon dioxide. In contrast, the low critical temperature associated to the dynamic diameter of N_2 (3.64 Å), which is higher than that of either O_2 (3.46 Å) or CO_2 (3.30 Å)[58], explains the lower permeability to nitrogen.

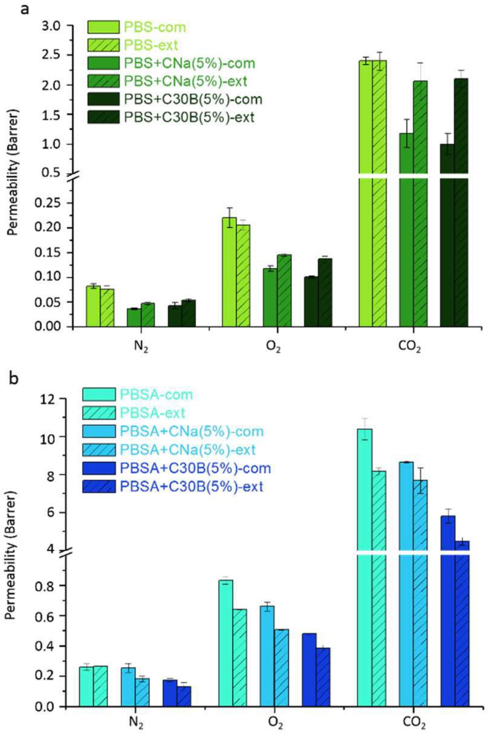

Figure 12 : Permeabilities to gases of the PBS-based films (a) and PBSA based films (b)

The permeation kinetics of gases (N_2, O_2, CO_2) revealed that the PBSA-based films are more permeable than the PBS-based films. This result is in accordance with the structures exhibited by the films. Indeed, crystals are usually considered to be impermeable entities that limit the diffusion of molecules through the film by tortuosity effects, and as a result a reduced permeability is obtained. It should be remembered that the crystals in the PBS-based films are larger and more numerous than in the PBSA-films, leading to an increase of diffusion pathways in the PBS-films, and hence, a reduced permeability to gases. The values gathered in Figure 12 show this clearly, irrespective of the gas molecule tested. Sinha Ray et al.[4] have measured the oxygen permeability of PBS at 20°C and 90% relative humidity and found 88 mL.mm.$m^{-2}day^{-1}MPa^{-1}$ corresponding to 0.14 Barrer. This value is quite close to ours (0.21 Barrer for PBS-ext and 0.22 Barrer for PBS-com) knowing that their lower value is probably due to the presence of the chain extender in PBS (0.48 wt%). By adding an organo-modified montmorillonite (C_{18}-mmt) in their PBS, they also observed a decrease of the oxygen permeability.

It can be noted that incorporating CNa into both matrices decreases the permeability to gas compared to the neat films (Figure 12). However, for the PBSA-based films, the lowest permeabilities are obtained when montmorillonite is organo-modified. This finding, reflecting improved barrier performances, can be related to structural effects. C30B platelets are indubitably more dispersed and delaminated in the PBSA matrix than CNa, as shown by TEM observations, XRD and rheological measurements, so more tortuous diffusing pathways are generated, causing stronger tortuosity effects, and this, associated to the stiffness of macromolecular chains in the vicinity of the fillers, leads to reduced permeability. For the PBS-based films, the permeabilities to gases are very similar, whatever the filler used. The higher crystallinity degree of PBS limits the effects of tortuosity brought by the nanoclays, which are found only in the amorphous phase; they are thus more confined than in the PBSA matrix. An illustration of how the composite structure affects the tortuosity is given in Scheme 1.

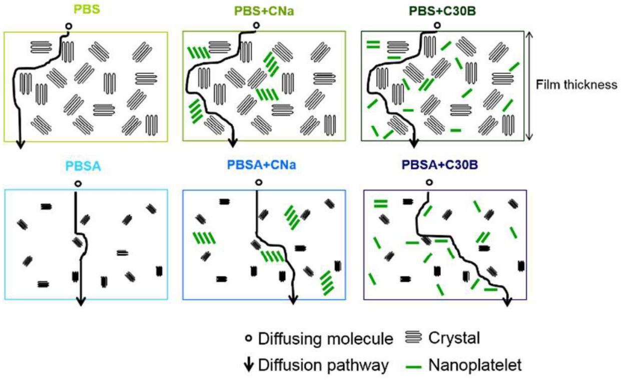

Scheme 1 : Representation of tortuosity effects induced in the PBS-based and PBSA-based films

Another interesting point arising from gas permeation results is the impact of the preparation process on the barrier properties of the composite films. For the PBSA-based films, the lowest gas permeabilities are obtained with the extrusion-calendering process. TEM images show that the extrusion-calendering process induces, under shearing forces, an orientation of the clays in the direction of the extrusion flow, where the platelets are aligned perpendicularly to the diffusing pathways. In addition to the orientation, the higher C30B dispersion and exfoliation levels, combined with the larger RAF, can be seen as synergistic effects responsible for a high increase in tortuosity, and as a result an improvement in the gas barrier properties.

The permeabilities of the unfilled PBS films are found to be very similar, whatever the film-forming process used. For the loaded PBS films, the gas barrier properties are better with the compression-molding process, even though the nanoclay orientation and better exfoliation observed in extruded PBS films led us to expect that the best performances would be obtained, as for PBSA films, with the extrusion-calendering process. In order to explain this result, we must remember that compression-molding favors RAF formation in the PBS films, as revealed by Flash-DSC experiments. Therefore, it is probable that, when the effects of the RAF are added to the effects of nanoclay exfoliation and orientation, this increases the barrier properties even more. This is a very interesting experimental result, because to our current knowledge such barrier properties have never been highlighted in the literature up to now.

However, contrary to loaded PBS films, in the case of unfilled PBS, PBS-com has a higher permeability in spite of a higher RAF. Thus, to understand this different trend of gas permeability between unfilled PBS and PBS composites, it becomes necessary to analyze more precisely the key parameters which influence the permeability.

As permeability is dependent on both diffusivity *D* and solubility *S* [10], it can be expressed by the $P = D \times S$ relationship, these two coefficients were determined for PBS and PBSA-based films and are presented in Figure 13 and Figure 14.

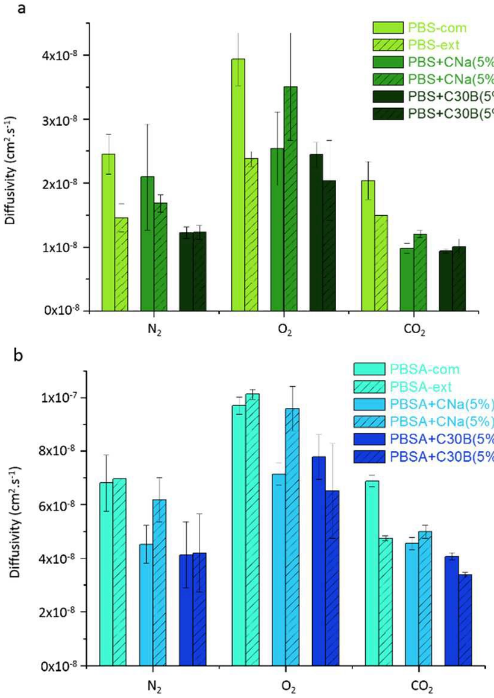

Figure 13 : Diffusivity of gas molecules in the PBS-based (a) and PBSA-based films (b).

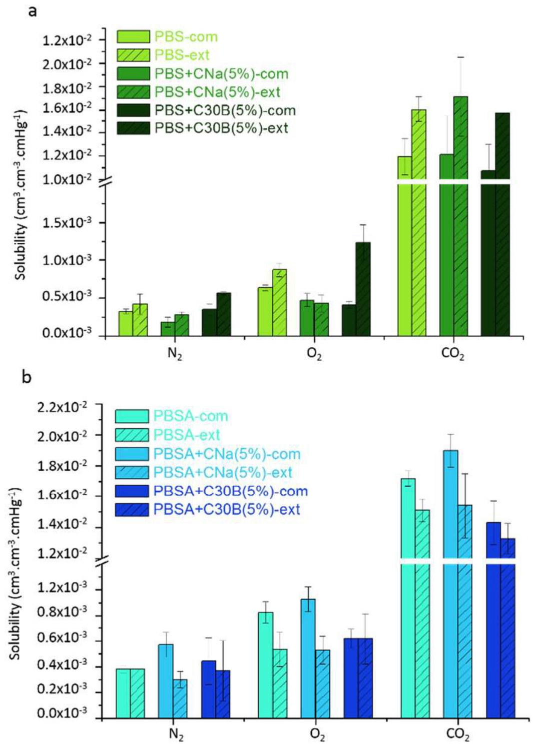

Figure 14 : Solubility gas molecules of the PBS-based (a) and PBSA-based films (b).

The gas diffusivity ranking can be mostly related to the Van der Waals volume of gas molecules. Indeed, it is usually postulated that a higher Van der Waals volume of a molecule induces a lower diffusion coefficient. This tendency is observed with our composite films, since the ranking *$D(CO_2) \leq D(N_2) \leq D(O_2)$* is obtained (Figure 13). The *D* ranking thus reflects the change in Van der Waals volumes of CO_2 (43.67 $cm^3.mol^{-1}$), N_2 (39.13 $cm^3.mol^{-1}$) and O_2 (31.83 $cm^3.mol^{-1}$)[59].

The CNa presence reduced the gas diffusivity in both the PBS and the PBSA matrices. This gas diffusivity is much more reduced by the presence of C30B. These results confirm the tortuosity increase induced by the nanofiller presence. As the permeability of the PBS+CNa and PBS+C30B films remained very similar (Figure 12), another parameter than the diffusivity should influence the permeability. Gas solubility can affect permeability by counterbalancing the diffusivity. We believe that in PBS, the diffusing molecule concentration in the loaded amorphous phase is less dependent on the dispersion state of fillers in comparison with PBSA, as there is less access in the PBS of lower amorphous phase fraction. However, as shown in Figure 14, a higher gas solubility is measured in the PBS+C30B films. This result can be correlated with the RAF/MAF ratio, as the gas solubility is probably lower in the RAF than in the MAF where the polymer chains were free to move. This result may seem very surprising when studies have reported an increase of permeant solubility with respect to the RAF in poly(ethylene terephthalate)[60] and in poly(lactic acid)[61]. These authors have explained the solubility increase by the presence of higher free volumes in the RAF than in the MAF due to the lower density of the RAF. PET and PLA, however, are in the glassy state at 25 °C so the free volumes in RAF are fixed and permanent, while in our case PBS and PBSA are in the rubbery state, where the free volumes present in the RAF are probably much less permanent. We also believe that the fewer permanent free volumes, along with the lower RAF mobility, hinder the solubility of permeant molecules.

Concerning the impact of the preparation process on gas diffusivity, no clear tendency was noted, whatever the polyester matrix. This result seems to indicate that the amount of RAF did not significantly increase the tortuosity, which is not surprising if we consider the size of the RAF which is generally taken to be small[47] in comparison with the adjacent crystalline and MAF phases. Gas solubility should also be affected by the preparation process. On the basis of a constant diffusion coefficient, solubility to N_2, O_2 and CO_2 was calculated for the prepared films (Figure 14). From these data, it is clear that the gas solubility was lower for the compressed than for the extruded-calendered PBS films, which had less RAF. On the contrary, the gas solubility of the PBSA films was higher for the compressed than for the extruded-calendered films, which had more RAF. Therefore, these experimental results demonstrate that the two preparation processes impact the microstructures of the PBS and PBSA composite films differently by promoting more or less RAF, which affects the resulting barrier performances. One key parameter to explain these results is the difference in the degree of crystallinity between the PBS and PBSA films (see **Table 2**). Indeed, in the amorphous phase of the PBSA films, which is clearly preponderant, the orientation of the polymer chains and inorganic platelets which was induced by shearing forces during the extrusion process is more easily maintained after cooling step as there is less crystalline zones for confining chains and platelets in PBSA than in PBS. Tortuosity effects are also increased by the presence of impermeable nanoclays and the RAF, which both improve barrier properties. In contrast, the PBS films are characterized by a reduced amorphous phase in which polymer chains are confined between crystals and nanofillers. This means that their capacity to move and to reorganize is limited when the crystallization occurs during the extrusion-calendaring. This phenomenon must be even more pronounced in presence of nanoplatelets. The compression molding seems to compact the PBS polymer chains and nanofillers, leading to RAF formation, where the rigidity of the polymer chains limits the solubility of gas molecules. Consequently, the barrier properties are improved.

For our PBSA films, which had a predominant amorphous phase, extrusion-calendering induced better nanoclay dispersion and exfoliation levels, with better oriented polymer chains, which resulted in better barrier properties than those obtained through compression-molding. Contrariwise, for the more crystalline PBS films, compression-molding seems to favor compaction of the crystals and nanoclays, and this effect on the barrier properties is apparently stronger than the effect of nanoclay orientation induced by extrusion-calendering.

However, for the unfilled PBS film, the opposite situation is observed as the PBS-com has a higher permeability in spite of having a higher RAF. Thus compression-molding will be less efficient in PBS without nanoclays so that the polymer chain orientation in PBS-ext would have more effects. These effects can be seen by a lower diffusivity for PBS-ext than for PBS-com. To confirm this result, complementary permeation measurements were done with water, another diffusing molecule.

Water transport properties

Water permeation kinetics enabled further investigation of the role played by the microstructure and by the RAF in the transport properties of the PBS and PBSA composite films. Water is a molecular probe of choice, as water molecules, unlike small gas molecules, are able to interact with the polymer and the montmorillonite. The water permeability results (Figure 15) usefully complement the gas barrier results.

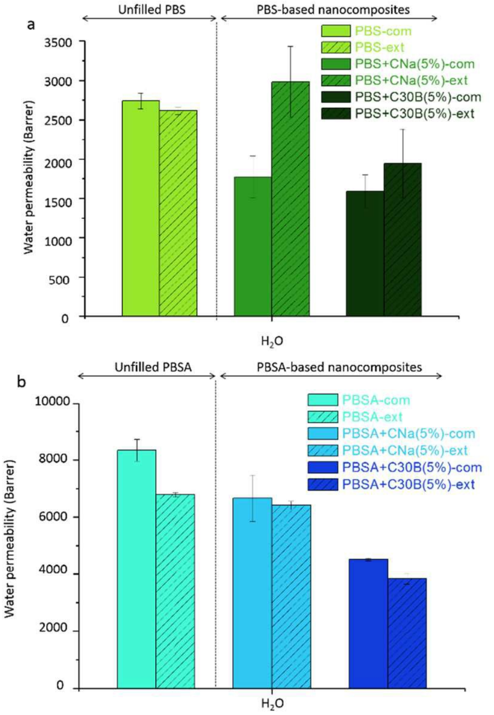

Figure 15 : Water permeability of the PBS-based films (a) and PBSA-based films (b)

As expected, the PBSA films were more permeable to water than the PBS films due to the higher crystallinity of PBS.

Compared to the unfilled PBS films, the presence of nanofillers in the PBS composite films decreased the water permeability. The one exception was the water permeability of the extruded-calendered PBS+CNa film, since it was found to be greater than for the unfilled PBS film. In fact, large nanoclay aggregates were observed in the extruded-calendered PBS+CNa film; they resulted from poor compatibility between the nanoclays and the matrix, which led to more free volumes at the filler-matrix interfaces. The combination of the high hydrophilicity of the filler and the free volumes at the surface of the clay aggregates probably induced a percolation effect that created preferential diffusing pathways for the water molecules. The water permeability of the other composite films followed the same trend as that observed with the gas molecules. Better water barrier properties were also obtained when incorporating CNa into the two matrices. The PBS+C30B films exhibit similar water barrier properties to the PBS+CNa films, while the PBSA+C30B films were characterized by better water barrier properties than the PBSA+CNa films, whatever the process used.

In the particular case of the unfilled PBS film, it is noteworthy that, as observed for gas results, the PBS-com has a higher permeability than PBS-ext in spite of its higher RAF. Also, as done with gas, in order to analyze the permeation behavior, the diffusivity has been determined.

Water, unlike gases, induces a plasticization phenomenon, and the diffusion coefficient dependence on the water concentration is clearly shown by the higher $D_{0.62}$ values compared to $D_{0.24}$ values

(Table 4). From the dependence law $D = D_0 . e^{\gamma . C}$(Equation 12) it was then possible to calculate the mean integral diffusion coefficient *<D>* (Equation 13) and the maximum diffusion coefficient D_M (Equation 14).

The tortuosity effects induced by the presence of nanofillers in the PBS and PBSA matrices decreased water diffusivity (Figure 16, Table 4). Moreover, the lowest diffusion coefficients were obtained in the films containing C30B, once again revealing better C30B dispersion and exfoliation levels compared with the films containing CNa. Furthermore, it is interesting to note that the diffusion coefficients calculated at different times of the permeation course, can be ordered as: $D_0 < D_{0.24} < D_{0.62} < D_M$, whatever the film, revealing water-induced plasticization effects exerted on both the polymer matrices.

Finally, the influence of the preparation process is clearly dependent on several factors impacting the polymer matrix. Extruding-calendering produced PBSA films with water barrier properties that were better than those obtained for the compressed films. For the PBS films, on the other hand, better water barrier properties were obtained with compression-molding than with extruding-calendering except for the unfilled PBS film. For this latter case, it is remarkable to see that, as observed with gas, a lower water diffusivity (Figure 15, Table 4) is obtained with the PBS-ext than with the PBS-com which has a higher RAF. Gas and water permeation results are thus consistent and would confirm that compression-molding applied on unfilled PBS has less effects on the barrier properties than the extrusion-calendering which promotes a chain orientation in PBS-ext. The presence of nanoclays in PBS would enhance the compaction effect in comparison with the orientation of chains.

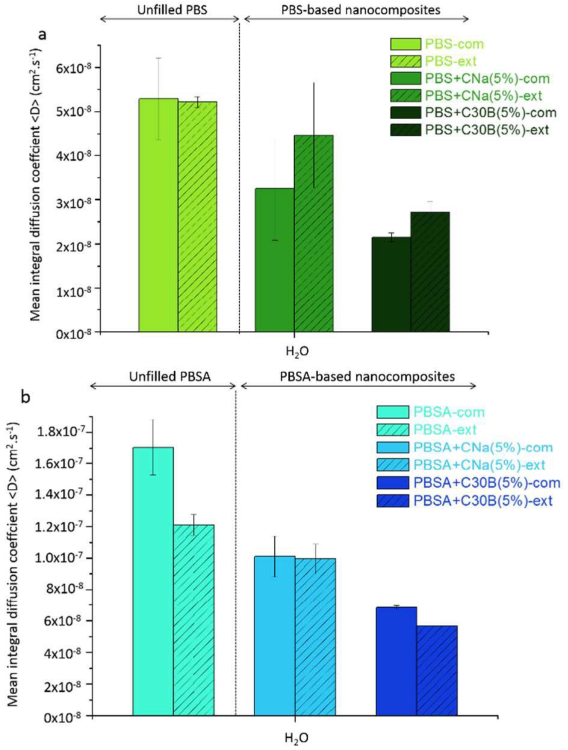

Figure 16 : Mean integral diffusion coefficient *<D>* of water in the PBS-based (a) and PBSA-based films (b)

Table 4 : Diffusion coefficients of water molecules in the PBS-based and PBSA-based films

	D_0x10^8 (cm^2.s^{-1})	$D_{0,24}$x10^8(cm^2.s^{-1})	$D_{0,62}$x10^8(cm^2.s^{-1})	D_Mx10^8(cm^2.s^{-1})
PBS-com	2,2 ± 0,1	3,1 ± 0,2	3,7 ± 0,4	11 ± 4
PBS+CNa(5%)-com	1,2 ± 0,1	1,8 ± 0,4	2,2 ± 0,6	7 ± 4
PBS+C30B(5%)-com	1,1 ± 0,1	1,4 ± 0,1	1,6 ± 0,1	4 ± 1
PBS-ext	1,6 ± 0,5	2,6 ± 0,4	3,3 ± 0,3	13 ± 2
PBS+CNa(5%)-ext	2,1 ± 0,4	2,8 ± 0,1	3,2 ± 0,3	9 ± 5
PBS+C30B(5%)-ext	1,6 ± 0,3	1,9 ± 0,1	2,0 ± 0,1	4 ± 1
PBSA-com	4,6 ± 0,9	8,1 ± 0,1	10,4 ± 0,3	43 ± 1
PBSA+CNa(5%)-com	3,4 ± 0,5	5,3 ± 0,1	6,6 ± 0,3	23 ± 6
PBSA+C30B(5%)-com	2,9 ± 0,4	4,0 ± 0,3	4,8 ± 0,3	14 ± 1
PBSA-ext	4,5 ± 0,7	6,6 ± 0,3	8,1 ± 0,1	26 ± 5
PBSA+CNa(5%)-ext	4,2 ± 0,4	5,7 ± 0,2	7,0 ± 0,3	20 ± 4
PBSA+C30B(5%)-ext	2,0 ± 0,1	3,0 ± 0,1	3,7 ± 0,1	13 ± 1

The water permeation results are in remarkably good agreement with those for the gases, despite the fact that new interactions occurred with the water molecules during the permeation process, and led to plasticization of the material. All the permeation data have clearly shown the influence of the microstructure on barrier properties, and the roles played by the crystalline phases and the constrained amorphous phases, especially, seem to be essential factors. The present study has shown that the complex microstructure properties of the PBS and PBSA composite films were well-correlated to the water and gas barrier properties. To our knowledge, there are no such results at the present time in the literature. Our complementary approach combining the analyses of the microstructure with the performances of the composite materials clearly demonstrates the value of permeation measurements as a means to probe matter at the molecular scale.

Conclusion

It is well-known that the amorphous part of semi-crystalline polymers cannot be view, for a large part of them, as a single phase. The three-phase model pointed out that a coupling interface exists between crystalline and amorphous parts and that a reduction of macromolecular mobility is one of the consequence. The novelty of this work is in the correlation of the transport properties with the composition of the amorphous phases (RAF/MAF ratio) in complex nanocomposite films composed of a bio-polyester (PBS or PBSA) and 5 wt% of clays (CNa or C30B). While the chemical structures of PBS and PBSA are very similar, their microstructures are clearly different, with a higher degree of crystallinity and larger spherulites for the PBS polyester in comparison with the PBSA, that explains the better barrier performances exhibited by the PBS films. We observed that an increase of the RAF leads systematically to a decrease of the permeant solubility in the film and consequently to a decrease of the film permeability, while the literature relates an increase of the permeant solubility when RAF increases in glassy polymers. In this study, four diffusing molecules (N_2, O_2, CO_2, H_2O) acting as molecular probes confirmed that their access is reduced in the RAF compared to the MAF at temperature Tg < T < Tg+70°C. The confinement of polymer chains in RAF induced two major effects which can mostly affect the transport properties of the material: the density is lower in RAF than in MAF while the polymer chains rigidity is higher in RAF than in MAF. Therefore, in glassy polymers like PET and PLA at 25 °C, more permanent free volumes exist in RAF than in MAF so that the solubility of permeants is higher in RAF than in MAF. In rubbery polymers like PBS and PBSA, the mobility of amorphous polymer chains (in MAF and in RAF) is higher than in glassy polymers and thereby no or very few permanent volumes must exist in RAF of rubbery polymers than of glassy polymers. We believe that the decrease of the molecular mobility locally induced by the presence of the RAF and the absence of permanent free volumes limit the access to diffusing species and so their solubilization in the RAF, which consequently improve the barrier properties of the materials. It was then possible to successfully explain all permeation results of nanocomposite films with the structure of the nanocomposites but also with the presence of the RAF which varies according to the structure of the matrix and the elaboration process. Indeed, if the presence of CNa or C30B has no effect on the degree of crystallinity of PBS or PBSA, it was interesting to observe that the gas and the water barrier properties of nanocomposites were dependent on the preparation process used. The barrier properties were improved for nanocomposite films having the higher RAF, ie: the PBS, nanocomposites prepared by compression-molding andthe PBSA nanocomposites prepared by extrusion-calendering. Concerning the role of the nanoclay chemistry, as expected, if the presence of the surfactant in C30B allows a better dispersion of fillers, it would also lead to an increase of the RAF but only in the PBSA matrix having a larger amorphous phase compared to PBS. For a better insight of the influence of the RAF on the transport properties, our next goal will be to investigate the molecular mobility through dielectric spectroscopy measurements.

Acknowledgements

The authors are greatly thankful to Dilys Moscato for her help in the English correction and to the French Ministry for Research and Technology for financial support.

References

[1] V.G.C. Gonzales, N. Machain, C. Campagna, *Mar. Pollut. Bull.*, 2015, **92**, 125-133.

[2] E.U.W. Péres, Jr.F. Comes de Souz, F.M. Silva, J.A. Chaker, P.A.Z. Suarez, *Ind. Crops Prod.*, 2014, **59**, 260-267.

[3] N. Follain, C. Chappey, E. Dargent, F. Chivrac, R. Crétois, S. Marais, *J. Phys. Chem. C.*, 2014, **118**, 6165-6177.

[4] S.S. Ray, K. Okamoto, M. Okamoto, *Macromolecules*, **36**, 2355-2367.

[5] J. Xu, B.H. Guo, *Biotechnology Journal*, 2010, **5**, 1149-1163.

[6] H.S. Kim, H.J. Kim, *Polym. Degrad. Stabil.*, 2008, **93**, 1544-1553.

[7] M.E. Makhatha, S.S. Ray, J. Hato, A.S. Luyt, M. Bousmina, *J. Nanosci. Nanothech.*, 2007, **8**, 1-11.

[8] Y.J. Phua, W.S. Chow, Z.A. Mohd Ishak, *Polym. Eng. Sci.*, 2013, **59**, 1947-1957.

[9] J.P. Jose, S. Thomas, Phys. Chem. Chem. Phys., 2014, 16, 14730-14740

[10] R. Crétois, N. Follain, E. Dargent, J. Soulestin, S. Bourbigot, S. Marais, L. Lebrun, Phys. Chem. Chem. Phys., 2015, **17**, 11313-11323

[11] F. Samyn, S. Bourbigot, C. Jama, S. Bellayer, *Polym. Degrad. Stabil.*, 2008, **93**, 2019-2024.

[12] K. Wilpiszewska, A. Krzysztof, T. Spychaj, *Carbohyd. Polym*., 2015, **128**, 82-89

[13] R. Wilson, N. Follain, N. Tenn, A. Kumar, S. Thomas, S. Marais, Phys. Chem. Chem. Phys., 2015, **17**, 19527-19537

[14] Z-Z. Tong, B. Zhou, J. Huang, J-T. Xu, Z-Q Fan, *Comp. Sci. Technol.*, 2013, **85**, 111-117.

[15] J.M. Cervantes-Uc, J.V. Cauich-Rodriguez, H. Vazquez-Torres, L.F. Garfias-Mesias, D.R. Paul, *Thermochim. Acta*, 2007, **457**, 92-102.

[16] T.D. Fornes, P.J. Yoon, D.R. Paul, *Polymer*, 2003, **44**, 7545-7556.

[17] S.P.B. Sousa, M.C.S. Ribeiro, J. Santos Baptista in *Occupational Safety and Hygyene II*, Ed. Taylor & Francis group, London, 2014, pp 25-29

[18] M.I. Carretero, C.S.F. Gomes, F. Tateo, in *Handbook of Clay Science*, Ed. F. Bergaya, B.K.G. Theng, G. Lagaly, Volume 1, 2006, pp 717-741

[19] L. Mészáros, T. Deák, G. Balogh, T. Czvikovszky, T. Czigány, *Comp. Sci. Technol.*, 2013, **75**, 22-27.

[20] H. Baniasadi, A. Ramazani, S. Javan Nikkhah, *Materials and Design*., 2010, **31**, 76-84.

[21] A. Rubio-Lopez, A. Olmedo, A. Diaz-Alvarez, C. Santiuste, *Comp. Struct*., 2015, 131, 995-1000.

[22] S. Lee, J. Yoo, J.W. Lee, *J. Ind. Eng. Chem*., 2015, **31**, 317-322.

[23] B. Alexandre, D. Langevin, P. Mederic, T. Aubry, H. Couderc, Q.T. Nguyen, A. Saiter, S. Marais, *J. Membr. Sci.*, 2009, **328**, 186-204.

[24] M.L. Di Lorenzo, R. Androsch, I. Stolte, *Polymer*, 2014, **55**, 6132-6139.

[25] F. Hamonic, V. Miri, A. Saiter, E. Dargent, *Eur. Polym. J.*, 2014, **58**, 233-244.

[26] S-K. Lim, J-J. Lee, S-G Jang, S-I. Lee, K-H. Lee, H-J Choi, I.J. Chin, *Polym. Eng. Sci.*, 2011, **51**, 1316-1324.

[27] S.S. Ray, J. Bandyopadhyay, M. Bousmina, *Eur. Polym. J.*, 2008, **44**, 3133-3145.

[28] J. Soulestin, B.J. Rashmi, S. Bourbigot, M-F. Lacrampe, P. Krawczak, *Macromol. Mater. Eng.*, 2012, **297**, 444-454

[29] N. Tenn, N. Follain, J. Soulestin, R. Crétois, S. Bourbigot, S. Marais, *J. Phys. Chem. C*, 2013, **117**, 12117-12135.

[30] Y.J. Phua, N.S. Lau, K. Sudesh, W.S. Chow, Z.A. Mohd Ishak, *Polym. Degrad. Stabil.*, 2012, **97**, 1345-1354.

[31] A. Dhotel, B. Rijal, L. Delbreilh, E. Dargent, A. Saiter, *J. Therm. Anal. Calorim.*, in press, 2015.

[32] C. Joly, D. Le Cerf, C. Chappey, D. Langevin, G. Muller, *Sep. Purif. Technol.*, 1999, **16**, 47-54.

[33] S. Marais, M. Métayer, Q.T. Nguyen, M. Labbé, D. Langevin, *Macromol. Theory Simul.*, 2000, **9**, 207-214.

[34] C.A. Kumins, T.K. Kwei, Ed. Crank, J.; Park, G. S. *Academic Press London and New York*, 135-137.

[35] S.V. Canevarolo, *Polym. Degrad. Stabil.*, 2000, **709**, 71-76.

[36] P. Bordes, E. Hablot, E. Pollet, L. Avérous, *Polym. Degrad. Stabil.*, 2009, **94**, 789-796.

[37] M. Ren, J. Song, C. Song, H. Zhang, X. Sun, Q. Schen, H. Zhang, Z. Mo, *J. Polym. Sci.: Part B: Polymer Physics*, 2005, **43**, 3231-3241.

[38] M.S. Nicolic, J. Djonlagic, *Polym. Degrad. Stabil.*, 2001, **74**, 263-270.

[39] Y.P. Khanna, W.P. Khun, *J. Polym. Sci.: Part B: Polymer Physics*, 1997, **35**, 2219-2231.

[40] I. Karacan, Fibers and Polymers, 2005, 6 (2005) 206-218.

[41] V. Tserki, P. Matzinos, E. Pavlidou, D. Vachliotis, C. Panayiotou, *Polym. Degrad. Stabil.*, 2006, **91**, 367-376.

[42] P. Pan, Z. Liang, N. Nakamura, T. Miyagawa, Y. Inoue, *Macromol. Biosci.*,2009, **9**, 585-595.

[43] J.A. Soto Puente, A. Esposito, F. Chivrac, E. Dargent, *Macromol. Symp.*, 2013, **328**, 8-19.

[44] X. Dai, Z. Zhang, C. Wang, Q. Ding, J. Jiang, K. Mai, *Comp. Sci. Technol.*, 2013, **89**, 38-43.

[45] K.E. Strawhecker, E. Manias, *Chem. Mater.*, 2003, **15**, 844-849.

[46] S.S. Ray, J. Bandyopadhyay, M. Bousmina, *Eur. Polym. J.*,2008, **44**, 3133-3145.

[47] Q. Zia, D. Mileva, R. Androsch, *Macromolecules*, 2008, **41**, 8095-8102.

[48] M.L. Di Lorenzo, M Gazzano, M.C. Righetti, *Macromolecules*, 2012, **45**, 5684-5691.

[49] K. Kuwabara, Z. Gan, T. Nakamura, H. Abe, Y. Doi, *Biomacromolecules*, 2002, **3**, 1095-1100.

[50] J. Bandyopadhyay, S-A. Al-Thabaiti, S.S. Ray, S.N. Basahel, M. Mokhtar, *Macromol. Mater. Eng.*, 2014, **299**, 939-952.

[51] N. Delpouve, A. Saiter, E. Dargent, *Eur. Polym. J.*, 2011, **47**, 2414-2423.

[52] M.C. Righetti, M. Laus, M. Di Lorenzo, *Eur. Polym. J.*, 2014, **58**, 60-68.

[53] X. Xu, Y. Ding, Z. Qian, F. Wang, B. Wen, H. Zhou, S. Zhang, M. Yang, *Polym. Degrad. Stabil.*, 2009, **94**,113-123.

[54] D. Chomat, J. Soulestin, M-F. Lacrampe, M. Sclavons, P. Krawczak, *J. Appl. Polym. Sci.*, 2015, **132**, 1-13.

[55] B. Vergnes, *Int. Polym. Process.*, 2011, **26**, 229-232.

[56] D.W. Van Krevelen, In *Properties of polymers*, 3rd edition, Elsevier, Amsterdam/Oxford, 1990

[57] D.R. Lide, *CRC Handbook of Chemistry and Physics*, 90th Edition, 2010, 957-960.

[58] R.W. Baker, J-G. Wijmans, Ed. D.R. Paul, Y.P. Yampol'skii, *CRC Press: Boca Raton*, Floride, 1994, 51.

[59] J.H. Petropoulos, Ed. D.R. Paul, Y.P. Yampol'skii, *CRC Press: Boca Raton*, Floride, 1994, 17-81.

[60] S. Lin, S. Shenogin, S. Nazarenko, *Polymer*, 2002, **43**, 4733-4743.

[61] M. Drieskens, R. Peeters, J. Mullens, D. Franlo, P.J. Lemstra, D.G. Hristova-Bogaerd, J. Polym. Sci.: Part B: *Polymer Physics*, 2009, **47**, 2247-2258.